

Flow-plane decorrelations in heavy-ion collisions with multiple-plane cumulants

Zhiwan Xu,^{1,*} Xiatong Wu,¹ Caleb Sword,² Gang Wang,^{1,†} Sergei A. Voloshin,² and Huan Zhong Huang^{1,3}

¹*Department of Physics and Astronomy, University of California, Los Angeles, California 90095, USA*

²*Department of Physics and Astronomy, Wayne State University, 666 W. Hancock, Detroit, Michigan 48201*

³*Key Laboratory of Nuclear Physics and Ion-beam Application (MOE), and Institute of Modern Physics, Fudan University, Shanghai-200433, People's Republic of China*

The azimuthal correlations between local flow planes at different (pseudo)rapidities (η) may reveal important details of the initial nuclear matter density distributions in heavy-ion collisions. Extensive experimental measurements of a factorization ratio (r_2) and its derivative (F_2) have shown evidence of the longitudinal flow-plane decorrelation. However, nonflow effects also affect this observable and prevent a quantitative understanding of the phenomenon. In this paper, to distinguish decorrelation and nonflow effects, we propose a new cumulant observable, T_2 , which largely suppresses nonflow. The technique sensitivity to different initial-state scenarios and nonflow effects are tested with a simple Monte Carlo model, and in the end, the method is applied to events simulated by a multiphase transport model (AMPT) for Au+Au collisions at $\sqrt{s_{NN}} = 200$ GeV. We also emphasize that a distinct decorrelation signal requires not only the right sign of an observable, but also its proper dependence on the η -window of the reference flow plane, to be consistent with the pertinent decorrelation picture.

keywords: flow decorrelation, nonflow

I. INTRODUCTION

Experiments on high-energy heavy-ion collisions, such as those at the BNL Relativistic Heavy Ion Collider (RHIC) and the CERN Large Hadron Collider (LHC), aim to create a quark gluon plasma (QGP) and to study the properties of this deconfined nuclear medium. Most heavy-ion collisions are not head-on, and traditionally, the nucleons experiencing at least one collision are considered as participants, and the remaining are labeled as spectators (see Fig. 1). While spectators fly away, the system created by the participant interaction presumably undergoes a hydrodynamic expansion. The initial geometry of the system is determined by the participant distribution, with event-by-event fluctuations. The pressure gradients of the medium convert the spatial anisotropies of the initial matter distribution into the momentum anisotropies of the final-state particles. Consequently, the azimuthal distributions of emitted particles can be analyzed with a Fourier expansion [1, 2]

$$\frac{dN}{d\varphi} \propto 1 + \sum_{n=1}^{\infty} 2v_n \cos[n(\varphi - \Psi^{\text{RP}})], \quad (1)$$

where φ denotes the azimuthal angle of a particle and Ψ^{RP} is the reaction plane azimuth (defined by the impact parameter vector). The Fourier coefficients,

$$v_n = \langle \cos[n(\varphi - \Psi^{\text{RP}})] \rangle, \quad (2)$$

are referred to as anisotropic flow of the n^{th} harmonic. By convention, v_1 , v_2 and v_3 are called “directed flow”,

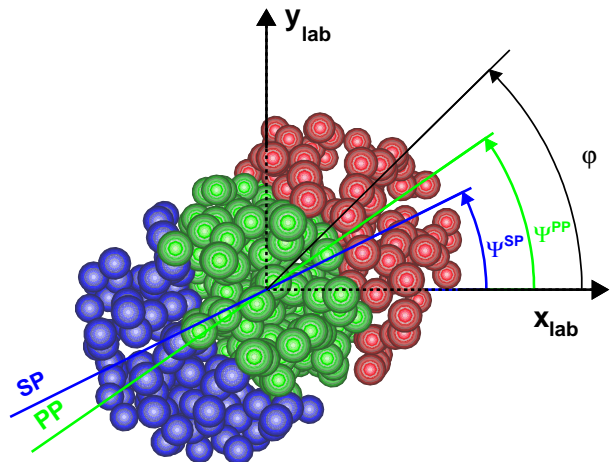


FIG. 1. (Color online) Schematic view of a two-nucleus collision in the transverse plane. The left nucleus is emerging from and the right one going into the page. Particles are produced in the overlap region (green-colored are the participant nucleons). The azimuthal angles of the spectator plane (Ψ^{SP}), the participant plane (Ψ^{PP}) and one of the produced particles (φ) are depicted here.

“elliptic flow”, and “triangular flow”, respectively. They reflect the hydrodynamic response of the system to the initial geometry (and its fluctuations) of the participant zone [3].

In reality, the reaction plane is unknown, and more importantly, the initial-state fluctuations drive the anisotropic flow along the planes that differ from the reaction plane, the so-called flow symmetry planes or participant planes (Ψ_n^{PP}). Then the particle azimuthal

* zhiwanxu@physics.ucla.edu

† gwang@physics.ucla.edu

distributions can be rewritten as

$$\frac{dN}{d\varphi} \propto 1 + \sum_{n=1}^{\infty} 2v_n \cos[n(\varphi - \Psi_n^{\text{PP}})]. \quad (3)$$

The meaning of the flow coefficients v_n changes from those in Eq. 2, but for simplicity of notations, the same symbols will be used, since in later discussions we will not determine the flow coefficients with the reaction plane. Anisotropic flow measurements relative to the participant plane are straightforward, as the flow itself can be used to estimate the corresponding flow plane. However, using the participant/flow plane also has its drawback – these planes become dependent on the kinematic region (rapidity and transverse momentum) of particles involved. This dependence is relatively weak, which still justifies the flow formalism of Eq. 3, but it needs to be taken into account to interpret high-precision flow measurements in modern experiments, especially the flow-plane decorrelation analyses to be discussed.

For clarity, we collect the definitions of different planes used in this paper below:

- Reaction plane (RP) is the plane spanned by the beam direction and the impact parameter vector. This plane is unique for every collision.
- Participant plane (PP) is defined by the initial density distribution. Subtle differences may exist, depending on, e.g., whether entropy or energy density is used as a weight, but these potentially small differences are not discussed in this paper. We assume that the properly constructed PPs define the development of anisotropic flow.
- Flow symmetry plane or flow plane (FP) determines the orientation of the corresponding harmonic anisotropic flow. It is assumed that FP coincides with the PP of the same harmonic (linear flow mode) or a proper combination of the lower harmonic PPs (nonlinear flow mode). With the nonlinear flow modes neglected, FP and PP are often used interchangeably.
- Event plane (EP) estimates the FP by analyzing the particle azimuthal distribution in a particular kinematic region. Owing to the finite number of particles involved in such an estimate, EP is subject to statistical fluctuations. The measurements obtained with EP have to be corrected for the event plane resolution [2], characterized by $\langle \cos[n(\Psi_n^{\text{EP}} - \Psi_n^{\text{FP}})] \rangle$. Ψ_n^{EP} is the azimuthal angle of the reconstructed n^{th} -harmonic flow vector, $\mathbf{Q}_n = (\sum_i^N w_i \cos(n\varphi_i), \sum_i^N w_i \sin(n\varphi_i))$, where w_i is the weight for each particle. For simplicity, we use unity weights in the event plane calculation.
- Spectator planes (SP) is determined by a sideward deflection of spectator nucleons, and is regarded as a better proxy for RP than FPs (determined by participants).

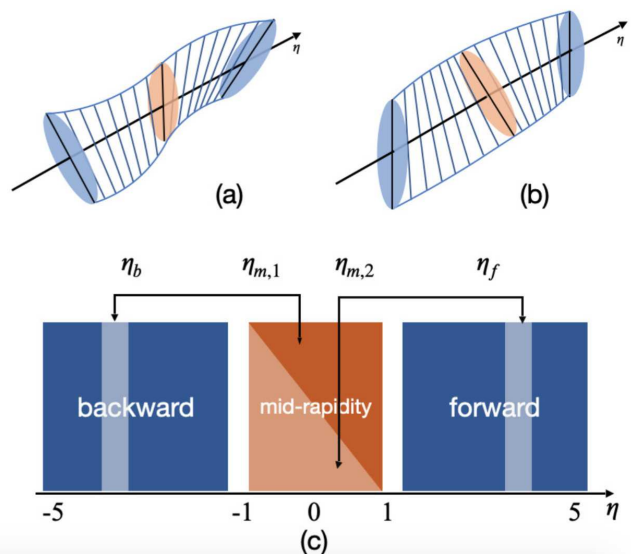


FIG. 2. (Color online) Schematic view of (a) the “torque” or S-shaped, and (b) the bow or C-shaped decorrelation patterns in the longitudinal distribution of the flow plane angle. The ellipses indicate the transverse momentum distributions of the final-state particles. Panel (c) delimits the kinematic regions for the particles at mid-, forward, and backward pseudorapidities.

The objective of this paper is the flow-plane decorrelation in the (pseudo)rapidity (η) direction. Decorrelation here means the deviation of a local flow plane from the value at the center-of-mass rapidity (y_{CM}), $\Delta\Psi(\eta) = \Psi(\eta) - \Psi(y_{\text{CM}})$. For simplicity, y_{CM} is set to zero for the symmetric collisions under study. In practice, we measure the relative tilt angles between the flow planes at backward, mid-, and forward rapidities. For concreteness we focus on the 2nd-harmonic flow. From event to event, two possible patterns arise from flow fluctuations: (a) when the flow plane angles at forward and backward pseudorapidities (Ψ_f and Ψ_b) fall on the opposite sides of the flow plane at midrapidity (Ψ_m) – the “torque” scenario, or S-shaped decorrelations, and (b) when Ψ_f and Ψ_b fall on the same side relative to Ψ_m – the “bow” scenario, or C-shaped decorrelations. These two cases are exemplified in panels (a) and (b) of Fig. 2, respectively.

The magnitude and pattern of the flow-plane decorrelation is extremely important, not only for the flow measurements (to be discussed in Sec. II), but also for understanding of the initial condition in the longitudinal direction. Flow-plane decorrelations can be caused by the torque effect [4], and more generally eccentricity decorrelations [5]. The mechanisms leading to the decorrelations also include hydrodynamic fluctuations in the QGP fluid [6] and glasma dynamics [7]. There also exists a phenomenological dynamical model of the initial states [8] that predicts the torque. We cannot exclude the possibility that the mechanisms causing the S-shaped decorre-

lations coexist with those originating the C-shaped ones in heavy-ion collisions. Therefore, experimental observables are only expected to measure the average effect and reveal the dominant decorrelation pattern.

A widely used measure of the longitudinal flow-plane decorrelation was introduced by the CMS Collaboration [9]:

$$r_n(\eta) = \frac{\langle \cos[n(\varphi_{-\eta} - \Psi_f)] \rangle}{\langle \cos[n(\varphi_\eta - \Psi_f)] \rangle} \quad (4)$$

$$= \frac{\langle v_n(-\eta) \cos[n(\Psi_{-\eta} - \Psi_f)] \rangle}{\langle v_n(\eta) \cos[n(\Psi_\eta - \Psi_f)] \rangle}, \quad (5)$$

with $\eta > 0$. Ψ_f can be replaced with Ψ_b , if η and $-\eta$ are simultaneously swapped in the definition. In a symmetric collision without any decorrelation, one would expect that $v(\eta) = v(-\eta)$ and the ratio to be unity. But if a torque pattern is present, with Ψ_f serving as a reference point, the decorrelation effect would be stronger for the negative-rapidity region, and the ratio would go below unity. Experimental data show that the factorization ratio r_2 indeed decreases with increasing η , and the deviation from unity is typically a few percent per unit pseudorapidity at both the LHC [9–11] and the RHIC [12]. Since both the flow-plane decorrelation and the flow-magnitude decorrelation can cause such a dependence of r_2 on η , efforts have been made to separate the two contributions [10, 13, 14]. However, before relating the observed $r_2(\eta)$ dependence to the flow-plane decorrelation, one has to examine an important physics background, the nonflow.

The nonflow effects are the correlations unrelated to the flow plane orientation or the initial geometry. Some nonflow effects are short-range in pseudorapidity, such as Coulomb and Bose-Einstein correlations (a few tenths of the unit of rapidity), resonance decays, and intra-jet correlations (about 1 unit rapidity), whereas back-to-back jets could contribute to the long-range correlations spanning over several units of rapidity. Therefore, even with a sizable η gap between an event plane and the particles of interest, one can not completely eliminate nonflow contributions to v_2 or r_2 measurements. Nonetheless, the numerator of r_2 does involve a larger η gap and hence a smaller nonflow contribution than its denominator, leading to a ratio smaller than unity, similar to that caused by the S-shaped flow-plane decorrelation. On the other hand, the C-shaped decorrelation may also be faked in experimental observables by nonflow effects such as back-to-back jet correlations.

In general, the decorrelation observables also depend on the η -window of the reference flow plane. In the following sections, we examine this dependence for various observables in the presence of nonflow and different types of flow-plane decorrelations. In Sec II, we use simple Monte Carlo simulations to demonstrate the impact of flow-plane decorrelations and nonflow on the v_2 measurements. Section III discusses the r_2 (and the closely related F_2 observable) analyses, and illustrates the possibilities of the η -differential measurements for a better in-

terpretation of the results. We show that nonflow effects tend to cause overestimation of F_2 , and to distort the $|\eta_{f(b)}|$ -dependence originally created by the flow-plane decorrelations. In Sec IV, we introduce a new four-plane observable, T_2 , which is essentially free from the nonflow contribution and has very distinct expectations for different decorrelation patterns. In Sec V, the developed techniques are applied to the Au+Au events generated by a multiphase transport (AMPT) model [15]. Finally in Sec VI, we summarize the findings and discuss the application of the new method to experimental data.

II. v_2 MONTE-CARLO SIMULATIONS

In elliptic flow measurements, it is a common practice to introduce a sizeable η gap between the event plane ($\Psi_{f(b)}$) and the particles of interest (φ_m) to suppress nonflow:

$$v_2\{\Psi_{f(b)}\} = \frac{\langle \cos[2(\varphi_m - \Psi_{f(b)})] \rangle}{\sqrt{\langle \cos[2(\Psi_f - \Psi_b)] \rangle}}, \quad (6)$$

where the denominator is the event plane resolution for $\Psi_{f(b)}$. Although both the numerator and the denominator are contaminated by nonflow, the latter is less affected because of a larger η gap between Ψ_f and Ψ_b . Therefore the effect of nonflow on $v_2\{\Psi_{f(b)}\}$ decreases with increasing the η gap or $|\eta_{f(b)}|$.

When the S-shaped flow-plane decorrelation is present, both the numerator and the denominator in Eq. 6 are reduced by the finite tilt angles due to the η gaps, and the denominator is more influenced because it involves an η gap larger than that of the numerator. Therefore, the S-shaped decorrelation tends to drive $v_2\{\Psi_{f(b)}\}$ above $v_2\{\Psi_{POI}\}$, where Ψ_{POI} is the event plane determined in the same η region as the particles of interest (POI).

To test these speculations, we perform a simple Monte Carlo simulation, where the tilt angle, $\Delta\Psi(\eta)$, is a linear function of η , with a slope of $\frac{d\Delta\Psi}{d\eta} = 1^\circ, 2^\circ, 3^\circ$ or 4° :

$$\Delta\Psi(\eta) \equiv \Psi(\eta) - \Psi(0) = \frac{d\Delta\Psi}{d\eta} \eta. \quad (7)$$

In our simulation (see Appendix A for details), each event has 1000 particles, distributed uniformly in the η range of $(-5, 5)$. The particle density $\frac{dN}{d\eta}|_{\eta=0} = 100$ corresponds roughly to the 30–50% centrality range in Au+Au collisions at $\sqrt{s_{NN}} = 200$ GeV, or 50–70% Pb+Pb at $\sqrt{s_{NN}} = 2.76$ TeV. The azimuthal angle of each particle has been assigned randomly according to the distribution of Eq. 3, and Ψ^{PP} is replaced with $\Psi(\eta)$. The POIs are selected within $|\eta| < 1$, and the $|\eta_{f(b)}|$ ranges used for calculations of Ψ_f and Ψ_b are taken from three bins: (2, 3), (3, 4) and (4, 5). For simplicity, the input v_2 is independent of η or transverse momentum (p_T), and the simulation does not include nonflow at this step. We implement a 15% flow fluctuation in all the following simple simulations, and observe no difference from

results with zero fluctuation. Figure 3(a) shows that the $v_2\{\Psi_{f(b)}\}/v_2\{\Psi_{POI}\}$ ratio is above unity, and increases with both $|\eta_{f(b)}|$ and $\frac{d\Delta\Psi}{d\eta}$, as expected for the S-shaped decorrelations. In the case of the C-shaped decorrelations, similar to Eq. 7, we assume

$$\Delta\Psi(\eta) = \frac{d\Delta\Psi}{d\eta}|\eta|, \quad (8)$$

and still vary $\frac{d\Delta\Psi}{d\eta}$ from 1° to 4° . Now that the tilt angle is symmetric around $\eta = 0$, the denominator in Eq. 6 is unchanged, and $v_2\{\Psi_{f(b)}\}$ tends to underestimate $v_2\{\Psi_{POI}\}$. Indeed, Fig. 3(b) shows that the $v_2\{\Psi_{f(b)}\}/v_2\{\Psi_{POI}\}$ ratio goes below unity, and decreases with increasing $|\eta_{f(b)}|$ and $\frac{d\Delta\Psi}{d\eta}$ for the C-shaped case. The ratios for the S-shaped and C-shaped scenarios can be well described, respectively, by

$$\frac{v_2\{\Psi_{f(b)}\}}{v_2\{\Psi_{POI}\}} = \frac{\cos(2\frac{d\Delta\Psi}{d\eta}|\eta_{f(b)}|)}{\sqrt{\cos(4\frac{d\Delta\Psi}{d\eta}|\eta_{f(b)}|)}} \quad (\text{S shape}), \quad (9)$$

$$\frac{v_2\{\Psi_{f(b)}\}}{v_2\{\Psi_{POI}\}} = \cos[2\frac{d\Delta\Psi}{d\eta}(|\eta_{f(b)}| - 0.5)] \quad (\text{C shape}). \quad (10)$$

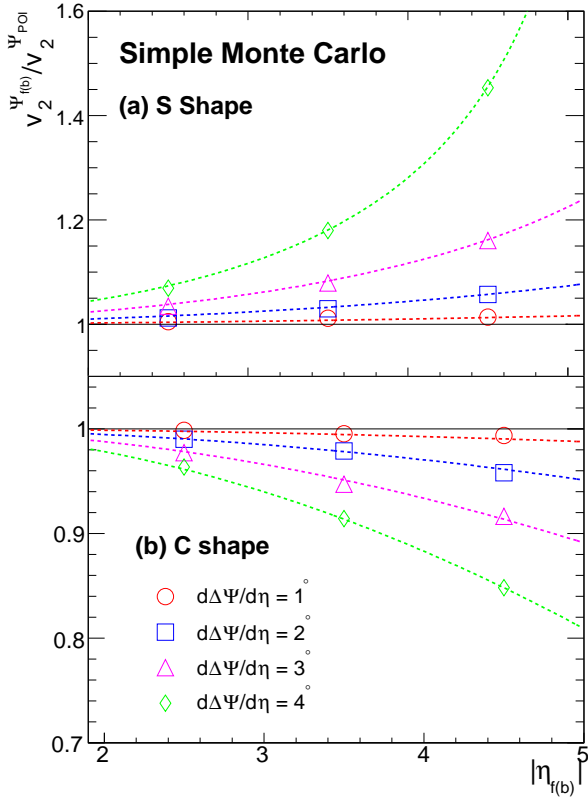


FIG. 3. (Color online) Simple Monte Carlo calculations of the ratio, $v_2\{\Psi_{f(b)}\}/v_2\{\Psi_{POI}\}$, without nonflow for the S-shaped (a) and the C-shaped (b) flow-plane decorrelations as a function of $|\eta_{f(b)}|$ and $\frac{d\Delta\Psi}{d\eta}$. The curves follow Eqs. (9) and (10).

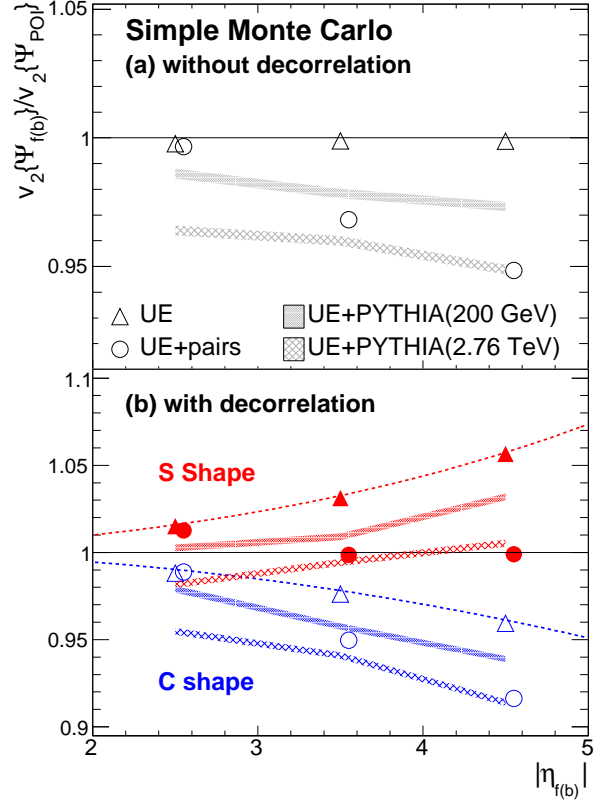


FIG. 4. (Color online) Simple Monte Carlo calculations of the $v_2\{\Psi_{f(b)}\}/v_2\{\Psi_{POI}\}$ ratio as a function of $|\eta_{f(b)}|$ for the underlying event (UE) without nonflow as well as for different scenarios of nonflow. $\frac{d\Delta\Psi}{d\eta}$ is set to 2° for the S-shaped and the C-shaped flow-plane decorrelations. The curves follow Eqs. 9 and 10 without nonflow. The shaded bands represent the two cases of PYTHIA embedding.

Therefore, to manifest a clear decorrelation signal, the v_2 ratio should go above unity with a rising trend vs $|\eta_{f(b)}|$ for a torque (S-shaped) case, or below unity with a falling trend for a bow (C-shaped) case.

We further implement nonflow correlations in the simulation, by adding to the “underlying” event (UE) pairs of particles with the same azimuthal angle. This nonflow simulation is similar to that used in Sec. IV(D) of Ref [16]. Note that since we deal with the 2^{nd} -harmonic flow, the near-side pairs with $\Delta\varphi \sim 0$ are equivalent to the away-side pairs with $\Delta\varphi \sim \pi$. One of the paired particles follows the uniform η distribution within $(-5, 5)$, and the other particle is separated with an η gap that obeys a Gaussian distribution with a width of 2 units of pseudorapidity. Four hundred paired particles (200 pairs) have been added to each underlying event. The simulated $v_2\{\Psi_{f(b)}\}/v_2\{\Psi_{POI}\}$ ratio is shown in Fig. 4 as a function of $|\eta_{f(b)}|$ with different amounts of nonflow. Panel (a) displays the scenario without any decorrelation, where nonflow fakes a falling trend. Panel (b) gives an example with $\frac{d\Delta\Psi}{d\eta} = 2^\circ$ for the S-shaped and the

C-shaped flow-plane decorrelations. In both scenarios, nonflow pulls down the original trends, and in the case of the S-shaped decorrelation, the initially rising trend could even be reversed into a falling one. Therefore, the $v_2\{\Psi_{f(b)}\}/v_2\{\Psi_{POI}\}$ ratio alone lacks discernment of different decorrelation scenarios.

Besides the simplified implementation of nonflow, which could exaggerate the effect, we also take a more realistic approach by embedding a few PYTHIA [17] events from p+p collisions at $\sqrt{s} = 200$ GeV or 2.76 TeV, such that PYTHIA particles replace the 400 paired particles (200 pairs). PYTHIA is an event generator that comprises a coherent set of physics mechanisms for the evolution from a few-body hard scattering process to a complex multihadronic final state. The corresponding results are shown with shaded bands in Fig. 4. The v_2 ratios thus obtained qualitatively show pull-down effects similar to the simplified nonflow case, with a stronger magnitude at the higher collision energy. In this study the embedding of PYTHIA particles into underlying events is done mostly to illustrate the effects of nonflow, but with parameters tuned to a specific centrality interval, it can also provide a quantitative estimate of nonflow contributions in the data analyses. More discussions on the simple Monte Carlo simulations and the nonflow effects can be found in Appendix A.

III. r_2 AND F_2

We define $r_2(\eta)$ based on Eq. 4 by setting $n = 2$. As suggested by Eq. 5, the deviation of r_2 from unity may originate from the decorrelations both in the flow-plane angles and in the v_2 magnitudes. Thus, we also examine the modified observable, r_2^Ψ [13], which is supposedly sensitive only to the flow-plane angles:

$$r_2^\Psi(\eta) = \frac{\langle \cos[2(\Psi_{-\eta} - \Psi_f)] \rangle}{\langle \cos[2(\Psi_\eta - \Psi_f)] \rangle}. \quad (11)$$

Experimentally as well as in model studies below, the dependence of $r_2^{(\Psi)}$ on η is almost linear, and the $F_2^{(\Psi)}$ slope is used to quantify the effect [9]:

$$r_2^{(\Psi)} = 1 - 2F_2^{(\Psi)}\eta. \quad (12)$$

We perform the linear- $\Delta\Psi(\eta)$ Monte Carlo simulation without nonflow to inspect the qualitative expectation of F_2 in the presence of the S-shaped flow-plane decorrelation. Note that in the C-shaped case, F_2 is zero by construction. In our simple simulations, F_2 and F_2^Ψ are always identical, so only the F_2 results are presented. Figure 5 depicts F_2 as a function of $|\eta_{f(b)}|$ and $\frac{d\Delta\Psi}{d\eta}$. F_2 increases with $\frac{d\Delta\Psi}{d\eta}$, since a larger tilt angle means a stronger torque. At first glance, it seems to be counter-intuitive that F_2 depends on the η location of the reference event plane, but the simulation actually reveals a

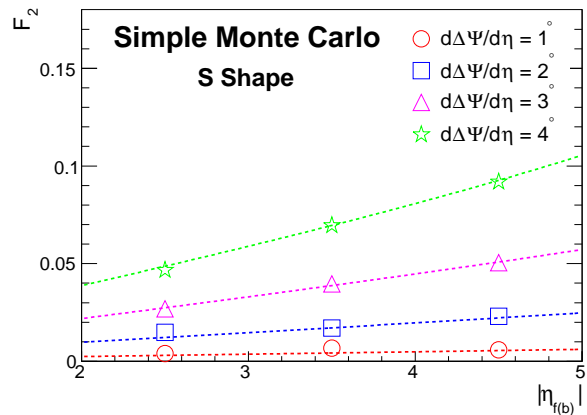


FIG. 5. (Color online) F_2 as a function of $|\eta_{f(b)}|$ and $\frac{d\Delta\Psi}{d\eta}$, from a simple Monte Carlo simulation for the S-shaped flow-plane decorrelation without nonflow. The curves reflect the analytical relation in Eq. 13.

simple mathematical relation:

$$1 - 2F_2\eta = \frac{\cos[2(\eta + |\eta_{f(b)}|)\frac{d\Delta\Psi}{d\eta}]}{\cos[2(\eta - |\eta_{f(b)}|)\frac{d\Delta\Psi}{d\eta}]}, \quad (13)$$

which yields $F_2 \approx 4(d\Delta\Psi/d\eta)^2|\eta_{f(b)}|$. Although in real collisions, the dependence of $\Delta\Psi$ on η may not be linear, we have verified with various monotonic function forms that the larger the η gap between POIs and the reference event plane is, the larger F_2 is. Thus an experimental observation of positive F_2 values with an increasing $F_2(|\eta_{f(b)}|)$ trend may reveal a distinct domination of the S-shaped flow-plane decorrelations.

In Fig. 6, nonflow contributions have been studied under the same framework as that used for the $v_2\{\Psi_{f(b)}\}/v_2\{\Psi_{POI}\}$ ratio. Since the simple simulation results on F_2 are the same for the scenarios with no decorrelation and with the C-shaped decorrelation, we use one set of data points to present both of them in panel (a). In these two scenarios, nonflow can fake a finite F_2 value, which decreases with increasing $|\eta_{f(b)}|$. Furthermore, panel (b) shows that nonflow not only quantitatively increases the magnitude of F_2 for the S-shaped decorrelation, but could also qualitatively change its rising trend into a falling one vs $|\eta_{f(b)}|$. The embedding of 400 PYTHIA particles resembles the simplified nonflow implementation with weaker effects, but finite F_2 values are still faked when the truth is no decorrelation or the C-shaped decorrelation. For the S-shaped decorrelation, the rising trend vs $|\eta_{f(b)}|$ is still distorted, especially at intermediate $|\eta_{f(b)}|$. Therefore, F_2 cannot unambiguously distinguish and quantify different decorrelation scenarios. Figure 2(a) of Ref. [11] gives a concrete example of such nonflow effects on the $|\eta_{f(b)}|$ dependence of F_2 in Xe+Xe collisions at $\sqrt{s_{NN}} = 5.44$ TeV.

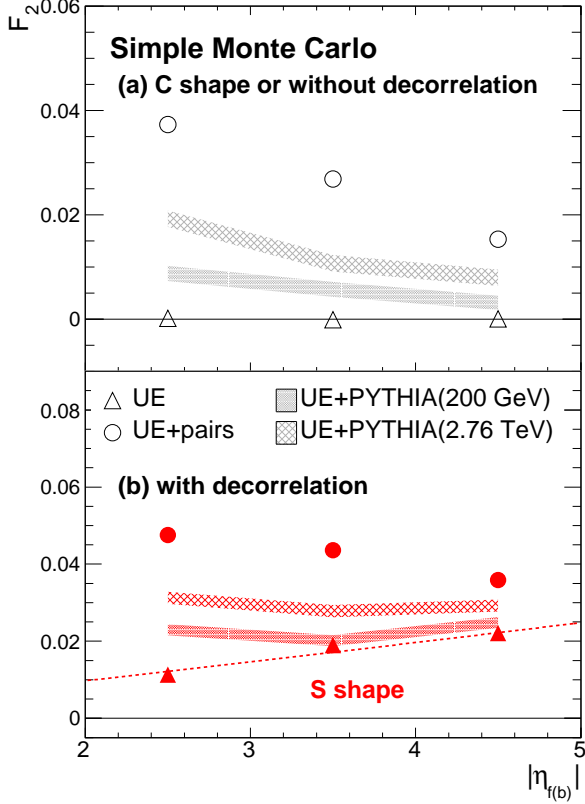


FIG. 6. (Color online) Simple Monte Carlo calculations of $F_2(|\eta_{f(b)}|)$ for the underlying event (UE) without nonflow as well as for different scenarios of nonflow. $\frac{d\Delta\Psi}{d\eta}$ is set to 2° for the S-shaped and the C-shaped flow-plane decorrelations. The curve follows the ideal relation in Eq. 13 without nonflow. The shaded bands represent the two cases of PYTHIA embedding.

IV. T_2 ANALYSES

In view of possible significant nonflow contributions in $v_2\{\Psi_{f(b)}\}$ and F_2 analyses, we advocate a new observable to probe the longitudinal flow-plane decorrelation:

$$T_2 = \frac{\langle\langle \sin 2(\Psi_f - \Psi_{m,1}) \sin 2(\Psi_b - \Psi_{m,2}) \rangle\rangle}{Res(\Psi_f)Res(\Psi_{m,1})Res(\Psi_b)Res(\Psi_{m,2})}, \quad (14)$$

where particles at midrapidities ($|\eta| < 1$) are divided into two sub-events to form $\Psi_{m,1}$ and $\Psi_{m,2}$, as demonstrated in Fig. 2(c). The double brackets denote ‘‘cumulant’’, and operate as follows:

$$\begin{aligned} & \langle\langle \sin(a-b) \sin(c-d) \rangle\rangle \\ &= \langle \sin(a-b) \sin(c-d) \rangle - \frac{1}{2} \langle \cos(a-c) \rangle \langle \cos(b-d) \rangle \\ & \quad + \frac{1}{2} \langle \cos(a-d) \rangle \langle \cos(b-c) \rangle, \end{aligned} \quad (15)$$

the derivation of which is elaborated in Appendix B. Taking into account the flow fluctuation contributions in the

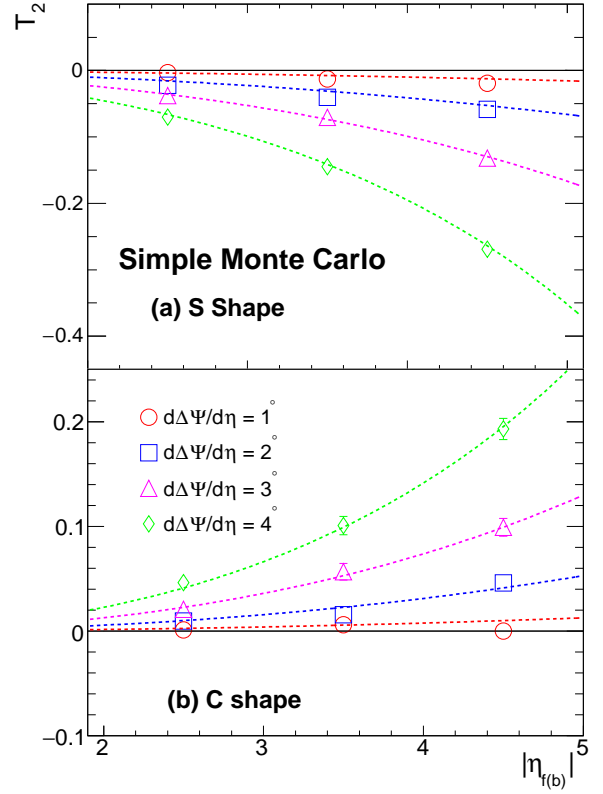


FIG. 7. (Color online) Simple Monte Carlo simulations of T_2 as a function of $|\eta_{f(b)}|$ and $\frac{d\Delta\Psi}{d\eta}$ for the S-shaped (a) and the C-shaped (b) flow-plane decorrelations without nonflow. The curves express Eqs. 17 and 18.

event plane resolution, we have

$$\begin{aligned} T_2 &= \frac{\langle \sin 2(\Psi_f - \Psi_{m,1}) \sin 2(\Psi_b - \Psi_{m,2}) \rangle}{\langle \cos 2(\Psi_f - \Psi_{m,1}) \cos 2(\Psi_b - \Psi_{m,2}) \rangle} \\ & \quad - \frac{\langle \cos 2(\Psi_f - \Psi_b) \rangle \langle \cos 2(\Psi_{m,1} - \Psi_{m,2}) \rangle}{2 \langle \cos 2(\Psi_f - \Psi_{m,1}) \rangle \langle \cos 2(\Psi_b - \Psi_{m,2}) \rangle} + \frac{1}{2} \end{aligned} \quad (16)$$

The generalization of the T_2 definition to four independent pseudorapidity ranges is straightforward and is discussed in Appendix C.

Defined as a four-particle cumulant, T_2 is essentially free from non-flow contribution (see Ref. [16] and references therein). T_2 , as expressed in Eq. 14, provides an intuitive way to tell whether Ψ_f and Ψ_b fall on the same side or the opposite sides of Ψ_m : a positive T_2 means a bow or a C-shaped decorrelation, and a negative T_2 signifies a torque or an S-shaped decorrelation. As done in the past, we shall exploit the linear- $\Delta\Psi(\eta)$ simulation without nonflow to learn the qualitative dependence of T_2 on $|\eta_{f(b)}|$ and $\frac{d\Delta\Psi}{d\eta}$ in different decorrelation patterns. With a specific $\frac{d\Delta\Psi}{d\eta}$, Fig. 7 shows a rapid decreasing trend of T_2 vs $|\eta_{f(b)}|$ for the S-shaped case in panel (a), and an increasing trend for the C-shaped case in panel (b). The simulated points obey the following mathematical rela-

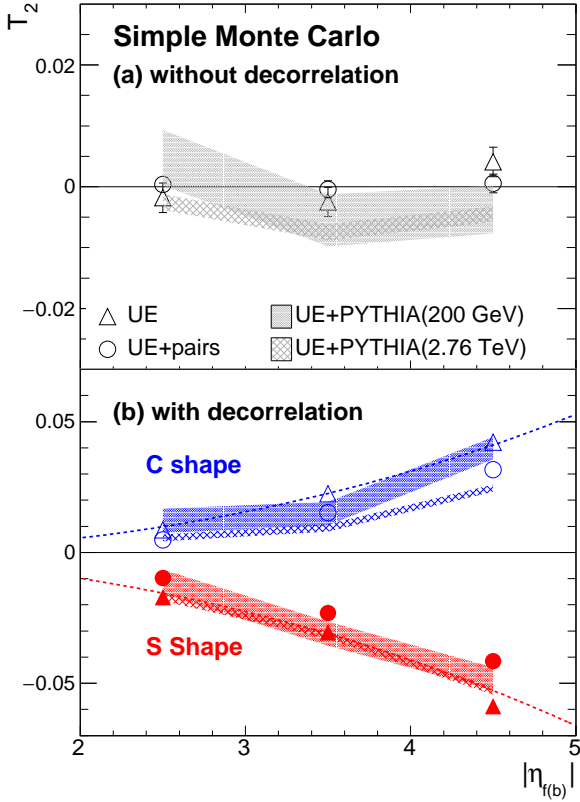


FIG. 8. (Color online) Simple Monte Carlo calculations of T_2 as a function of $|\eta_{f(b)}|$ for the underlying event (UE) without nonflow as well as for different scenarios of nonflow. $\frac{d\Delta\Psi}{d\eta}$ is set to 2° for the S-shaped and the C-shaped flow-plane decorrelations. The curves manifest Eqs. 17 and 18 without nonflow. The shaded bands represent the two cases of PYTHIA embedding.

tions:

$$T_2 = -\frac{\sin^2(2\frac{d\Delta\Psi}{d\eta}|\eta_{f(b)}|) + \frac{1}{2}\cos(4\frac{d\Delta\Psi}{d\eta}|\eta_{f(b)}|)}{\cos^2(2\frac{d\Delta\Psi}{d\eta}|\eta_{f(b)}|)} + \frac{1}{2}$$

$$= -\frac{1}{2}\tan^2(2\frac{d\Delta\Psi}{d\eta}|\eta_{f(b)}|) \text{ (S shape),} \quad (17)$$

$$T_2 = \frac{\sin^2[2\frac{d\Delta\Psi}{d\eta}(|\eta_{f(b)}| - 0.5)] - \frac{1}{2}}{\cos^2[2\frac{d\Delta\Psi}{d\eta}(|\eta_{f(b)}| - 0.5)]} + \frac{1}{2}$$

$$= \frac{1}{2}\tan^2[2\frac{d\Delta\Psi}{d\eta}(|\eta_{f(b)}| - 0.5)] \text{ (C shape).} \quad (18)$$

Again, in reality, the tilt angle may not increase linearly with the η gap, but we have confirmed with various monotonic function forms that the falling and rising trends of T_2 vs $|\eta_{f(b)}|$ should be solid expectations for the S-shaped and the C-shaped decorrelations, respectively.

In $v_2\{\Psi_{f(b)}\}$ and F_2 analyses, the core element is a cosine function that yields large values close to 1 in strong-nonflow scenarios. Conversely, T_2 uses the cumulant of a sine function that gives close-to-zero nonflow contributions. Nonflow studies on T_2 are presented in Fig. 8 with

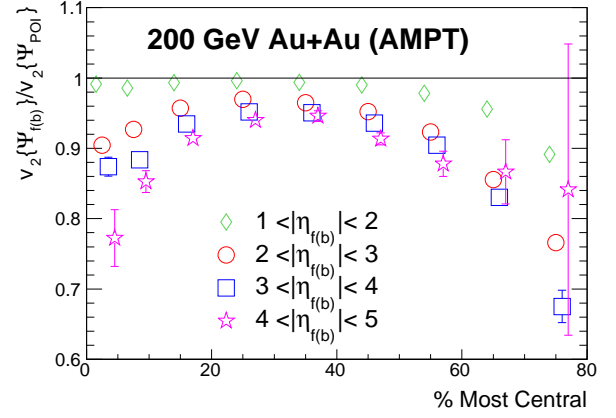


FIG. 9. (Color online) AMPT calculations of the $|\eta_{f(b)}|$ dependence of the $v_2\{\Psi_{f(b)}\}/v_2\{\Psi_{POI}\}$ ratio in different centrality intervals of Au+Au collisions at $\sqrt{s_{NN}} = 200$ GeV. Results using Ψ_f and Ψ_b are combined. Some points are staggered horizontally to improve visibility.

the same procedure as before. Panel (a) shows that for the scenario without any decorrelation, the T_2 results are mostly consistent with zero, with a potential of slightly negative values with the embedding of PYTHIA events at 2.76 TeV. Panel (b) shows that for the scenarios with the C-shaped and the S-shaped decorrelations, the T_2 magnitude could be slightly reduced by nonflow, but the original trends are not changed vs $|\eta_{f(b)}|$.

V. AMPT STUDIES

We test the aforementioned methodology with more realistic events, simulated by the AMPT model [15]. AMPT is a hybrid transport event generator, and describes four major stages of a high-energy heavy-ion collision: the initial conditions, the partonic evolution, the hadronization, and the hadronic interactions. For the initial conditions, AMPT uses the spatial and momentum distributions of minijet partons and excited soft strings, as adopted in the Heavy Ion Jet Interaction Generator (HIJING) [18]. Then Zhang's parton cascade [19] is deployed to manage the partonic evolution, determined by the two-body parton-parton elastic scattering. At the end of the partonic evolution, the hadronization is implemented via the spatial quark coalescence. Finally, the hadronic interactions are modeled by a relativistic transport calculation [20]. The string-melting (SM) version of AMPT reasonably well reproduces particle spectra and elliptic flow in Au+Au collisions at $\sqrt{s_{NN}} = 200$ GeV and Pb+Pb collisions at 2.76 TeV [21]. In this study, Au+Au collisions at 200 GeV are simulated by the SM version v2.25t4cu of AMPT.

In the following analyses of the AMPT events, we only select π^\pm , K^\pm , p and \bar{p} with $0.15 < p_T < 2$ GeV/c. φ_m and Ψ_m are delimited with $|\eta| < 1$, and Ψ_f and Ψ_b

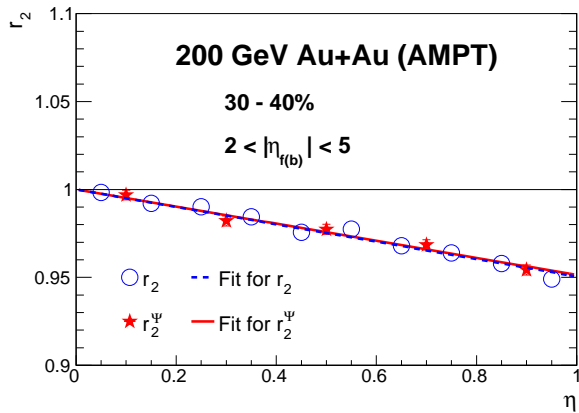


FIG. 10. (Color online) $r_2(\eta)$ and $r_2^\Psi(\eta)$ in 30-40% Au+Au collisions at $\sqrt{s_{NN}} = 200$ GeV, simulated by AMPT. Results using Ψ_f and Ψ_b are combined. The straight-line fits to the r_2 and r_2^Ψ points extract the corresponding F_2 of $(2.47 \pm 0.11) \times 10^{-2}$ and F_2^Ψ of $(2.43 \pm 0.11) \times 10^{-2}$.

are reconstructed with particles within $2 < \eta < 5$ and $-5 < \eta < -2$, respectively. With the expectations from nonflow and the scenarios of flow-plane decorrelations in mind (see Figs. 3 and 4), we examine the $|\eta_{f(b)}|$ dependence of the $v_2\{\Psi_{f(b)}\}/v_2\{\Psi_{POI}\}$ ratio in AMPT. Figure 9 shows the AMPT calculations of this ratio for four $|\eta_{f(b)}|$ bins in different centrality intervals of Au+Au collisions at $\sqrt{s_{NN}} = 200$ GeV. Within each centrality bin, $v_2\{\Psi_{f(b)}\}/v_2\{\Psi_{POI}\}$ displays a decreasing trend with the increasing η gap, excluding the S-shaped decorrelation from the dominant underlying mechanisms. Both nonflow and the C-shaped decorrelation could induce such a decreasing trend in the v_2 ratio, and we cannot yet discern the two scenarios using this observable.

Next, the AMPT results of $r_2(\eta)$ and $r_2^\Psi(\eta)$ are compared in Fig. 10 for 30-40% Au+Au collisions at 200 GeV.

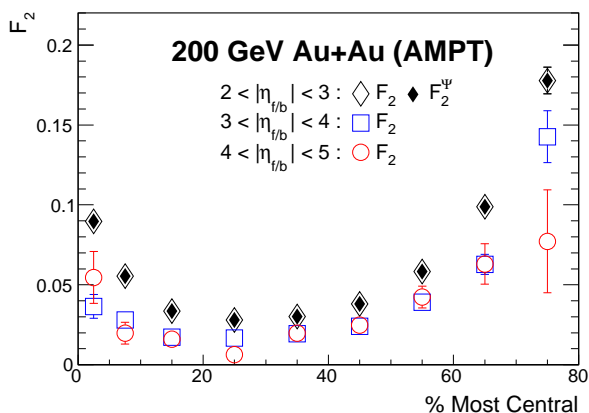


FIG. 11. (Color online) F_2 and F_2^Ψ for different $\eta_{f/b}$ ranges as functions of centrality in Au+Au collisions at $\sqrt{s_{NN}} = 200$ GeV from AMPT.

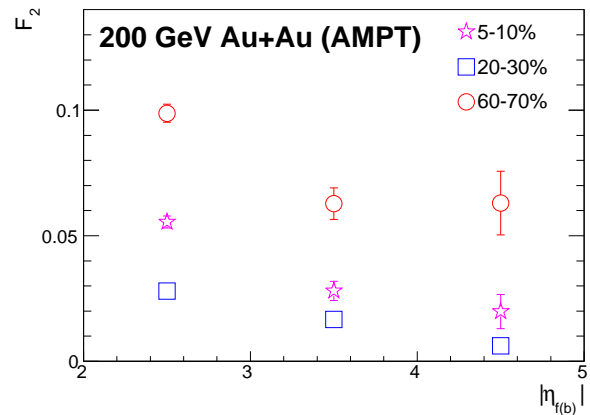


FIG. 12. (Color online) AMPT calculations of F_2 versus $|\eta_{f(b)}|$ for three selected centrality ranges in Au+Au collisions at $\sqrt{s_{NN}} = 200$ GeV.

As mentioned earlier, Ψ_f can be replaced with Ψ_b in the r_2 definition, with η and $-\eta$ simultaneously exchanged. The two sets of results have been combined to gain better statistics. Both r_2 and r_2^Ψ show a linear trend decreasing as η increases, seemingly indicating a torque in the flow-plane decorrelation at midrapidities. The linear fits render the very close values of $F_2 = (2.47 \pm 0.11) \times 10^{-2}$ and $F_2^\Psi = (2.43 \pm 0.11) \times 10^{-2}$, which implies a marginal contribution of v_2 -magnitude decorrelations at midrapidities in AMPT events.

Figure 11 presents the AMPT calculations of F_2 and F_2^Ψ for different $\eta_{f/b}$ ranges as a function of centrality. The two quantities are very close to each other in most centrality bins, and to avoid clutter, we only show F_2^Ψ for the case of $2 < |\eta_{f/b}| < 3$ as a demonstration. Thereafter, we focus on F_2 . For the three $|\eta_{f/b}|$ ranges, the magnitude of F_2 is about 2.5% in the 10–50% centrality range, and becomes larger in more central and more peripheral events. Before attributing the finite F_2 values to the flow-plane decorrelation, one should note that such a centrality dependence could be a reflection of nonflow effects. Nonflow contributions are positive in F_2 , and become more pronounced in peripheral collisions where multiplicity is low and in central collisions where v_2 is small. This caveat also applies to experimental data [9, 12] that show F_2 features similar to these AMPT simulations. Moreover, the F_2 dependence on $|\eta_{f/b}|$ and centrality qualitatively resembles Fig.2(a) of Ref. [11], corroborating the nonflow contribution.

The qualitative expectation from the simple Monte Carlo simulation (see Figs. 5 and 6) motivates the differential measurements of F_2 with respect to $|\eta_{f(b)}|$. Figure 12 delineates AMPT calculations of F_2 as a function of $|\eta_{f(b)}|$ for three selected centrality bins in Au+Au collisions at 200 GeV. The F_2 values are positive for all the cases under study, consistent with the S-shaped decorrelation. However, the $|\eta_{f(b)}|$ dependence shows a falling trend in each centrality interval, in contrast to the ris-

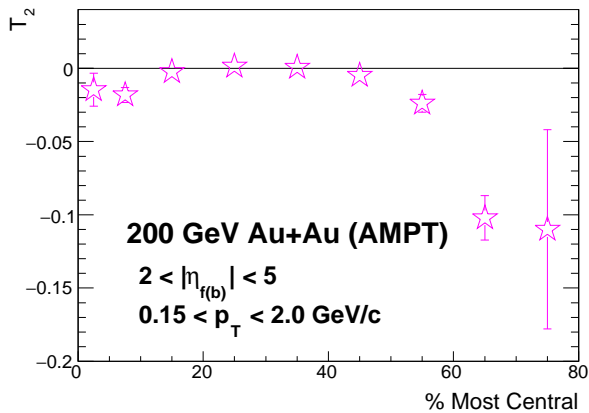


FIG. 13. (Color online) Centrality dependence of T_2 in AMPT events of Au+Au collisions at $\sqrt{s_{NN}} = 200$ GeV. The $|\eta_{f(b)}|$ range is (2, 5) for Ψ_f and Ψ_b .

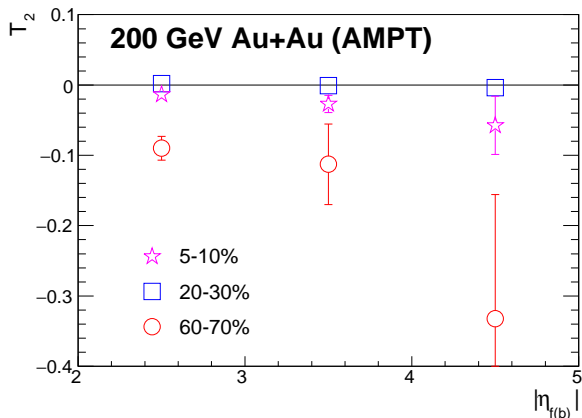


FIG. 14. (Color online) T_2 dependence on $|\eta_{f(b)}|$ for three selected centrality ranges in AMPT events of Au+Au at $\sqrt{s_{NN}} = 200$ GeV.

ing trend expected for the torque alone. Therefore, the contribution of the S-shaped flow-plane decorrelation in these F_2 values, if any, must have been dominated by nonflow effects, which are also positive, and decrease with increasing $|\eta_{f(b)}|$.

Finally, Fig. 13 depicts the T_2 values as a function of centrality in the AMPT events of Au+Au collisions at 200 GeV. For the 10–50% centrality range, T_2 is consistent with zero, indicating no apparent flow-plane decorrelation. In more central or more peripheral events, T_2 falls negative, supporting the picture of a torque or the S-shaped decorrelation. Note that when the tilt angle between Ψ_m and $\Psi_{f(b)}$ becomes large, the denominator of T_2 significantly under-estimates the product of the event-plane resolutions, which in turn will blow up the magnitudes of both T_2 and its statistical uncertainty. This effect partially attributes to the large T_2 magnitudes and the large error bars in peripheral collisions. The bright side is that this effect does not change the sign of T_2 , be-

TABLE I. AMPT results of T_2 and F_2 for $2 < |\eta_{f(b)}| < 5$ from Figs. 11 and 13 as well as the corresponding tilt angles ($\frac{d\Delta\Psi}{d\eta}$) versus centrality in Au+Au collisions at 200 GeV. $\frac{d\Delta\Psi}{d\eta}$ is extracted using Eqs. 13, 17 and 18 without nonflow. For the tilt angles from T_2 , a minus sign is added, if the decorrelation is C-shaped.

% central	F_2 (%)	T_2 (%)	$\frac{d\Delta\Psi}{d\eta}\{F_2\}$ ($^\circ$)	$\frac{d\Delta\Psi}{d\eta}\{T_2\}$ ($^\circ$)
0-5	7.0 (0.4)	-1.5 (1.1)	4.26 (0.13)	1.3 (0.9)
5-10	4.3 (0.2)	-1.8 (0.5)	3.37 (0.09)	1.7 (0.2)
10-20	2.6 (0.1)	-0.2 (0.2)	2.61 (0.06)	0.5 (0.4)
20-30	2.1 (0.1)	0.1 (0.2)	2.35 (0.06)	-0.4 (0.5)
30-40	2.6 (0.1)	0.1 (0.2)	2.57 (0.06)	-0.2 (0.6)
40-50	3.1 (0.1)	-0.5 (0.3)	2.84 (0.06)	0.8 (0.3)
50-60	4.9 (0.2)	-2.4 (0.6)	3.57 (0.08)	1.9 (0.2)
60-70	8.1 (0.4)	-10.2 (1.5)	4.58 (0.10)	3.8 (0.3)
70-80	16.0 (0.9)	-11.0 (6.8)	6.42 (0.17)	3.6 (1.7)

cause the denominator is always positive by symmetry.

The AMPT results of T_2 as a function of $|\eta_{f(b)}|$ are plotted in Fig. 14 for three selected centrality bins in Au+Au collisions at 200 GeV. For the 20–30% centrality range, T_2 is always consistent with zero, whereas for 5–10% and 60–70% collisions, there seem to be decreasing trends due to a torque, although the statistical uncertainties become large at increased $|\eta_{f(b)}|$. Therefore, both the sign and the $|\eta_{f(b)}|$ -dependence of T_2 confirm the S-shaped longitudinal decorrelation in central and peripheral AMPT events.

A comparison between F_2 and T_2 is possible, if we neglect nonflow effects for the moment, and use Eqs. 13, 17 and 18 to extract the tilt angles from these two observables. Table I lists the values of F_2 and T_2 as a function of centrality for $2 < |\eta_{f(b)}| < 5$ from Figs. 11 and 13, as well as the extracted tilt angles. The average $|\eta_{f(b)}|$ is around 3.2 with a weak centrality dependence. In general, the tilt angles obtained from F_2 have magnitudes larger than those from T_2 , and the difference could be attributed to contributions other than nonflow. The smaller tilt-angle values obtained from T_2 might also indicate a stochastic nature of the flow-plane decorrelations as a function of $\Delta\eta$. For example, one can model the flow-plane angle along the longitudinal direction with a Markov chain: the η range is divided into many small steps, and the flow plane at each step is randomly tilted by a small amount with respect to that at the previous step. In that case $\langle(\Delta\Psi)^2\rangle \propto \Delta\eta$. Such a random-walk-like process will lead to a positive F_2 independent of $|\eta_{f(b)}|$, but have zero contribution to T_2 .

VI. CONCLUSIONS

The flow-plane azimuthal decorrelations provide important input to the initial condition and the system evolution of heavy-ion collisions in the longitudinal dimension. We have explored three analyses that may be sensitive to such decorrelations: $v_2\{\Psi_{f(b)}\}/v_2\{\Psi_{POI}\}$,

$F_2^{(\Psi)}$ and T_2 . Using simple Monte Carlo simulations with a constant $\frac{d\Delta\Psi}{d\eta}$ slope, we have learned the impacts of decorrelation and nonflow on these observables as functions of $|\eta_{f(b)}|$.

- In the absence of nonflow, the $v_2\{\Psi_{f(b)}\}/v_2\{\Psi_{\text{POI}}\}$ ratio will increase(decrease) with increasing $|\eta_{f(b)}|$, if the decorrelation is S-shaped(C-shaped). However, nonflow tends to pull down the trend, and could cause a falling trend even with the S-shaped decorrelation.
- Without nonflow, F_2 is zero in the case of the C-shaped decorrelation or no decorrelations, and is positive, increasing with $|\eta_{f(b)}|$ in the S-shaped case. Again, nonflow could force a decreasing trend regardless of whether the decorrelation is a torque or a bow.
- $T_2(|\eta_{f(b)}|)$ is expected to distinguish the C-shaped and the S-shaped decorrelation patterns with opposite trends. Nonflow could slightly reduce the magnitude of T_2 , but is unlikely to change the pertinent trend.

We have further applied the aforementioned methods to the AMPT events of Au+Au collisions at $\sqrt{s_{\text{NN}}} = 200$ GeV. The findings are summarized in the following.

- For each centrality interval under study, the $v_2\{\Psi_{f(b)}\}/v_2\{\Psi_{\text{POI}}\}$ ratio decreases with increasing $|\eta_{f(b)}|$, which means that the S-shaped decorrelation cannot be the dominant underlying mechanism for this observable. This approach is unable to separate nonflow from the C-shaped decorrelation.
- F_2 and F_2^Ψ are very close to each other in most cases, indicating a negligible v_2 -magnitude decorrelation in AMPT. It is of interest to see if that is also true in experimental data.
- Although the positive sign of $F_2^{(\Psi)}$ seems to evidence the torque in AMPT, nonflow contributions cast a shadow over this interpretation, with the decreasing trend of $F_2(|\eta_{f(b)}|)$.
- The novel observable, T_2 , suppresses nonflow with the sine function and the cumulant treatment. T_2 is consistent with no decorrelation for 10–50% AMPT events of Au+Au at 200 GeV, and supports the S-shaped decorrelation picture in 0–10% and 50–80% collisions, with both the right sign and the expected $|\eta_{f(b)}|$ -dependence.

We have demonstrated the importance of the $|\eta_{f(b)}|$ dependence of the experimental observables for the interpretation in terms of flow-plane decorrelations. The proposed T_2 observable exhibits advantages over the v_2 ratio and F_2 with regard to nonflow effects, and is sensitive to details of the decorrelation patterns tracing back to the initial participant matter. Although we concentrate

on the 2nd-harmonic flow, the methodology presented in this paper can be readily extended to higher harmonics. We look forward to the corresponding applications to the real-data analyses.

ACKNOWLEDGMENTS

The authors thank Zi-Wei Lin and Guo-Liang Ma for providing the AMPT code. We thank Maowu Nie, Jiangyong Jia, Aihong Tang, ShinIchi Esumi and Mike Lisa for the fruitful discussions. Z. Xu, X. Wu, G. Wang and H. Huang are supported by the U.S. Department of Energy under Grant No. DE-FG02-88ER40424. C. Sword and S. Voloshin are supported by the U.S. Department of Energy Office of Science, Office of Nuclear Physics under Grant No. DE-FG02-92ER40713.

Appendix A: Two-particle correlations in the simple simulation

The nonflow effects can be easily visualized in the correlation function between two particles, $\delta_2 \equiv \langle \cos[2(\varphi_1 - \varphi_2)] \rangle$, as a function of their η gap ($\Delta\eta$). Without nonflow or decorrelation, δ_2 simply reflects $\langle v_2^2 \rangle$. Figure 15(a) presents $\delta_2(\Delta\eta)$ for four distinct classes of particles without decorrelation in the simple Monte Carlo simulation. The 1000 particles in each underlying event uniformly cover the η range of $(-5, 5)$, and carry an average v_2 of 5%. From event to event, v_2 follows a uniform distribution from 3.5% to 6.5%. Since the underlying events are free of nonflow, the corresponding δ_2 remains constant at $\langle v_2^2 \rangle + \sigma^2$, where $\sigma \sim 0.75\%$ is due to the event-by-event fluctuation. The second class consists of 400 paired particles without elliptic flow. Within each of the 200 pairs, the two particles have the same azimuthal angle, and their $\Delta\eta$ follows a Gaussian distribution with zero mean and a width of 2 units of η . Although the mean values of δ_2 are almost identical for the 1000 underlying-event particles and the 400 paired particles, the $\Delta\eta$ dependence is very different between these two cases. The former is constant, whereas the latter is enhanced at small $\Delta\eta$, and approaches zero at large η gaps. The result from the simple nonflow implementation qualitatively resembles the correlation between the 400 PYTHIA particles (triangular markers), with stronger effects. On average, the combination of 21(12) single PYTHIA events of p+p collisions at 200 GeV(2.76 TeV) provides the 400 PYTHIA particles. Although a single PYTHIA event has very strong nonflow effects as shown in panel (b), the correlation strength is diluted roughly by a factor of 21 or 12, when such a number of PYTHIA events are merged together. Interestingly, the single PYTHIA events of different collision energies illustrate similar long-range correlations at $\Delta\eta > 1$. Finally, panel (c) shows the correlation results after the “nonflow” particles are embedded into the underlying events. In general, the embedded events display

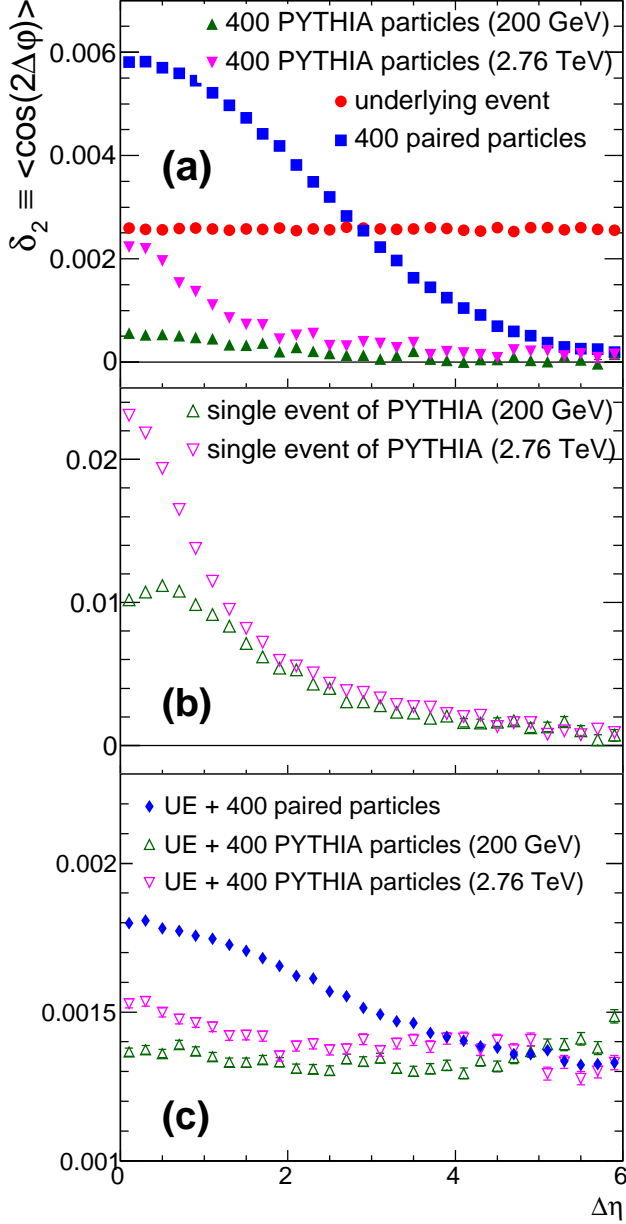


FIG. 15. (Color online) δ_2 as a function of $\Delta\eta$ for different classes of particles in the simple Monte-Carlo simulations. Panel (a) includes the underlying event without nonflow, the simple nonflow implementation with 400 paired particles, and two cases of 400 PYTHIA particles from p+p collisions at $\sqrt{s} = 200$ GeV and 2.76 TeV, respectively. The results from single PYTHIA events are presented in panel (b).

lower δ_2 values than the underlying events, since the 400 particles with no flow dilute the 1000 flowing particles. Meanwhile, nonflow correlations cause the nonuniform $\Delta\eta$ dependence. In practice, the simple Monte Carlo simulation can be tuned to compare with real data, and help us understand the nonflow contributions.

Appendix B: Cumulant of four-angle correlations

The two-variable cumulant of an observable, $f = xy$, is defined as

$$\langle\langle xy \rangle\rangle \equiv \langle xy \rangle - \langle x \rangle \langle y \rangle. \quad (\text{B1})$$

The first term computes the average of the product, accounting for correlations between x and y , while the second gives the product of the averages, keeping x and y independent of each other. A zero cumulant means that x and y are independent with no correlation. The T_2 observable involves four azimuthal angles, and therefore we derive the four-variable cumulant, which subtracts all lower-order correlations:

$$\begin{aligned} \langle\langle xyzt \rangle\rangle &\equiv \langle xyzt \rangle - \langle\langle xyz \rangle\rangle \langle t \rangle - \langle\langle xyt \rangle\rangle \langle z \rangle \\ &\quad - \langle\langle xzt \rangle\rangle \langle y \rangle - \langle\langle yzt \rangle\rangle \langle x \rangle - \langle\langle xy \rangle\rangle \langle\langle zt \rangle\rangle \\ &\quad - \langle\langle xz \rangle\rangle \langle\langle yt \rangle\rangle - \langle\langle xt \rangle\rangle \langle\langle yz \rangle\rangle \\ &\quad - \langle x \rangle \langle y \rangle \langle z \rangle \langle t \rangle. \end{aligned} \quad (\text{B2})$$

In principle, we should obtain the three-variable cumulants before calculating the four-variable cumulant. However, in the case of T_2 , all the variables can be expressed as a sine or cosine function of an azimuthal angle, and we can force $\langle x \rangle = \langle y \rangle = \langle z \rangle = \langle t \rangle = 0$ in the data analyses, e.g., via the shifting method [22]. Thus, Eq. B2 is simplified to

$$\langle\langle xyzt \rangle\rangle = \langle xyzt \rangle - \langle xy \rangle \langle zt \rangle - \langle xz \rangle \langle yt \rangle - \langle xt \rangle \langle yz \rangle. \quad (\text{B3})$$

The numerator of T_2 can be expanded into four terms:

$$\begin{aligned} &\sin(a-b) \sin(c-d) \\ &= \sin(a) \cos(b) \sin(c) \cos(d) \\ &\quad - \sin(a) \cos(b) \sin(d) \cos(c) \\ &\quad - \sin(b) \cos(a) \sin(c) \cos(d) \\ &\quad + \sin(b) \cos(a) \sin(d) \cos(c). \end{aligned} \quad (\text{B4})$$

We put the first term into Eq. B3 as an example,

$$\begin{aligned} &\langle\langle \sin(a) \cos(b) \sin(c) \cos(d) \rangle\rangle \\ &= \langle\langle \sin(a) \cos(b) \sin(c) \cos(d) \rangle\rangle \\ &\quad - \langle\langle \sin(a) \sin(c) \rangle\rangle \langle\langle \cos(b) \cos(d) \rangle\rangle, \end{aligned} \quad (\text{B5})$$

where terms such as $\langle\langle \sin(a) \cos(b) \rangle\rangle$ vanish in symmetric heavy-ion collisions. Using the product-to-sum formulas, we have

$$\begin{aligned} &\langle\langle \sin(a) \sin(c) \rangle\rangle \langle\langle \cos(b) \cos(d) \rangle\rangle \\ &= \frac{1}{4} [\langle\langle \cos(a-c) \rangle\rangle \langle\langle \cos(b-d) \rangle\rangle \\ &\quad + \langle\langle \cos(a+c) \rangle\rangle \langle\langle \cos(b+d) \rangle\rangle \\ &\quad - \langle\langle \cos(a-c) \rangle\rangle \langle\langle \cos(b-d) \rangle\rangle \\ &\quad - \langle\langle \cos(a+c) \rangle\rangle \langle\langle \cos(b+d) \rangle\rangle]. \end{aligned} \quad (\text{B6})$$

Only the cosines with arguments of the angle difference are independent of the coordinate system, and may render finite averages. Hence Eq. B5 becomes

$$\begin{aligned} & \langle \langle \sin(a) \cos(b) \sin(c) \cos(d) \rangle \rangle \\ &= \langle \sin(a) \cos(b) \sin(c) \cos(d) \rangle \\ & - \frac{1}{4} \langle \cos(a-c) \rangle \langle \cos(b-d) \rangle. \end{aligned} \quad (\text{B7})$$

We follow the same procedure for the other three terms in Eq. B4 and obtain

$$\begin{aligned} & \langle \langle \sin(a-b) \sin(c-d) \rangle \rangle \\ &= \langle \sin(a-b) \sin(c-d) \rangle - \frac{1}{2} \langle \cos(a-c) \rangle \langle \cos(b-d) \rangle \\ & + \frac{1}{2} \langle \cos(a-d) \rangle \langle \cos(b-c) \rangle. \end{aligned} \quad (\text{B8})$$

Appendix C: Generalization of T_2

In the T_2 analyses in Sec. IV, we randomly split particles within $|\eta| < 1$ into two sub-events, and reconstruct $\Psi_{m,1}$ and $\Psi_{m,2}$ based on them. By this means, $\Psi_{m,1}$ and $\Psi_{m,2}$ are indistinguishable, sharing the same kinematic region, bearing the same event plane resolution, and tilting in the same way. In general, $\Psi_{m,1}$ and $\Psi_{m,2}$ could come from different η ranges, e.g., with $-1 < \eta_{m,1} < 0$ and $0 < \eta_{m,2} < 1$. Accordingly, the definition of T_2 is not unique any more, with a few possible combinations. For example, we can define

$$T_{2(I)} = \frac{\langle \langle \sin 2(\Psi_f - \Psi_{m,2}) \sin 2(\Psi_b - \Psi_{m,1}) \rangle \rangle}{\langle \cos 2(\Psi_f - \Psi_{m,2}) \rangle \langle \cos 2(\Psi_b - \Psi_{m,1}) \rangle}, \quad (\text{C1})$$

and within the frame work of the simple Monte Carlo simulation, where the tilt angle linearly increases with the η gap, we have

$$T_{2(I)} = -\frac{1}{2} \tan^2 \left[2 \frac{d\Delta\Psi}{d\eta} (|\eta_{f(b)}| - 0.5) \right] \text{ (S shape),} \quad (\text{C2})$$

$$T_{2(I)} = \frac{1}{2} \tan^2 \left[2 \frac{d\Delta\Psi}{d\eta} (|\eta_{f(b)}| - 0.5) \right] \text{ (C shape).} \quad (\text{C3})$$

We can switch $\Psi_{m,1}$ and $\Psi_{m,2}$ in $T_{2(I)}$ to define a new observable

$$T_{2(II)} = \frac{\langle \langle \sin 2(\Psi_f - \Psi_{m,1}) \sin 2(\Psi_b - \Psi_{m,2}) \rangle \rangle}{\langle \cos 2(\Psi_f - \Psi_{m,1}) \rangle \langle \cos 2(\Psi_b - \Psi_{m,2}) \rangle}, \quad (\text{C4})$$

and with the constant $\frac{d\Delta\Psi}{d\eta}$, we have

$$T_{2(II)} = -\frac{1}{2} \tan^2 \left[2 \frac{d\Delta\Psi}{d\eta} (|\eta_{f(b)}| + 0.5) \right] \text{ (S shape)} \quad (\text{C5})$$

$$T_{2(II)} = \frac{1}{2} \tan^2 \left[2 \frac{d\Delta\Psi}{d\eta} (|\eta_{f(b)}| - 0.5) \right] \text{ (C shape).} \quad (\text{C6})$$

A third type of T_2 observable can be defined as

$$T_{2(III)} = \frac{\langle \langle \sin 2(\Psi_f - \Psi_b) \sin 2(\Psi_{m,1} - \Psi_{m,2}) \rangle \rangle}{\langle \cos 2(\Psi_f - \Psi_b) \rangle \langle \cos 2(\Psi_{m,1} - \Psi_{m,2}) \rangle}, \quad (\text{C7})$$

which is zero for the C-shaped decorrelation. With the constant $\frac{d\Delta\Psi}{d\eta}$, the expectation from the S-shaped case is

$$T_{2(III)} = -\frac{1}{2} \tan \left(2 \frac{d\Delta\Psi}{d\eta} \right) \tan \left(4 \frac{d\Delta\Psi}{d\eta} |\eta_{f(b)}| \right). \quad (\text{C8})$$

-
- [1] S. Voloshin and Y. Zhang, Z. Phys. C **70**, 665 (1996).
 - [2] A. M. Poskanzer and S. A. Voloshin, Phys. Rev. C **58**, 1671 (1998).
 - [3] U. Heinz and R. Snellings, Ann. Rev. Nucl. Part. Sci. **63**, 123 (2013).
 - [4] P. Bozek, W. Broniowski, and J. Moreira, Phys. Rev. C **83**, 034911 (2011).
 - [5] A. Behera, M. Nie, and J. Jia, (2020), Phys. Rev. Res. **2**, 023362 (2020).
 - [6] L.-G. Pang, G.-Y. Qin, V. Roy, X.-N. Wang, and G.-L. Ma, Phys. Rev. C **91**, 044904 (2015).
 - [7] B. Schenke and S. Schlichting, Phys. Rev. C **94**, 044907 (2016).
 - [8] Shen, Chun and Schenke, Bjorn, Phys. Rev. C **97**, 024907 (2018).
 - [9] V. Khachatryan *et al.* [CMS Collaboration], Phys. Rev. C **92**, 034911 (2015).
 - [10] M. Aaboud *et al.* [ATLAS Collaboration], Eur. Phys. J. C **78**, 142 (2018).
 - [11] G. Aad *et al.* [ATLAS Collaboration], Phys. Rev. Lett. **126**, 122301 (2021).
 - [12] M. Nie [STAR Collaboration], Nucl. Phys. A **1005**, 121783 (2021).
 - [13] P. Bozek and W. Broniowski, Phys. Rev. C **97**, 034913 (2018).
 - [14] A. Sakai, K. Murase, T. Hirano, Phys. Rev. C **102**, 064903 (2020).
 - [15] Z.-W. Lin, C.M. Ko, B.-A. Li, B. Zhang, S. Pal, Phys. Rev. C **72**, 064901 (2005).
 - [16] C. Adler *et al.* [STAR Collaboration], Phys. Rev. C **66**, 034904 (2002).
 - [17] T. Sjostrand, S. Mrenna, and P. Z. Skands, JHEP **05**, 026 (2006).
 - [18] X.-N. Wang and M. Gyulassy, Phys. Rev. D **44**, 3501 (1991).
 - [19] B. Zhang, Comput. Phys. Commun. **109**, 193 (1998).
 - [20] B. A. Li and C. M. Ko, Phys. Rev. C **52**, 2037 (1995).
 - [21] Zi-Wei Lin, Phys. Rev. C **90**, 014904 (2014).
 - [22] J. Barrette *et al.* [E877 Collaboration], Phys. Rev. C **56**, 3254 (1997).